Sarker et al. *Microsystems & Nanoengineering* (2025)11:171
https://doi.org/10.1038/s41378-025-01005-2

Microsystems & Nanoengineering
www.nature.com/micronano

ARTICLE Open Access

3D nanoprinting of embryo microinjection needles with anti-clogging features

Sunandita Sarker[1,2,3,4]✉, Ziteng Wen[1], Ruben Acevedo[1], Andrew C. Lamont[5], Adira Colton[1], Lucas Kieran Muller[1], DoHwan Park[6], Eleonora Tubaldi[1,2,3,7], Kinneret Rand-Yadin[8] and Ryan D. Sochol[1,2,3,5,7]✉

Abstract

Wide-ranging biomedical applications spanning both research and clinical settings rely on microinjection protocols that involve using a long, hollow microneedle to deliver foreign substances directly into biological targets, such as embryos. Unfortunately, conventional microneedles are prone to clogging—e.g., cytoplasmic material from an embryo becoming lodged inside the needle tip during penetration, thereby obstructing delivery—motivating researchers to use top-down microfabrication techniques to modify needle tips and reduce such failure modes. Recent advancements for the submicron-scale additive manufacturing approach, "Two-Photon Direct Laser Writing (DLW)", offer a new, bottom-up pathway for re-architecting microneedle tips to address clogging susceptibility via geometric means. Here, we investigate this potential by 3D printing monolithic 650-µm-tall, 15-µm-diameter hollow microneedles comprising architectural features designed to remediate clogging phenomena: (i) a solid, fine-point tip, (ii) multiple side ports (i.e., perpendicular to the insertion direction), and (iii) an internal microfilter. Serial microinjection experiments with live zebrafish embryos reveal that the 3D microneedles yield enhanced delivery performance without any instances of complete blockages that are pervasive among both standard glass and 3D-printed control microneedles. These findings suggest that DLW-based 3D printing holds distinctive promise for high-precision microinjection applications, particularly in scenarios involving extensive serial injections or critical payloads and targets.

Introduction

Microinjection techniques underlie a diversity of biomedical applications ranging from fundamental research in fields including cell, systems, and developmental biology, stem cell gene manipulation, intracytoplasmic sperm injection (ICSI), and disease modeling as well as medical procedures such as in vitro fertilization (IVF), pre-implantation genetic diagnosis, and intraocular injection[1–4]. Hollow microneedles—also referred to as "micropipettes", "microcapillary needles", and "microcapillary pipettes"—are fundamental to microinjection protocols as the primary vehicle for delivering small volumes of external substances, such as cells, DNA, RNA, proteins, viruses, and micro/nanoparticles, directly into biological targets including cells, embryos, tissues, organs, and organisms[5–7]. Historically, the vast majority of these microneedles have comprised architectures that include a tapered needle tip with a singular orifice located at the top of the tip[8–10]. Because the single opening is directly in line with the microneedle's insertion direction, such needle geometries are intrinsically prone to undesired clogging phenomena wherein material from the injection target becomes lodged inside the tip as the microneedle initially punctures and penetrates into the target prior to delivery[11–16]. Correspondingly, the success of broad microinjection processes can be negatively affected by microneedle clogging, which can reduce injection efficiencies, increase injection-to-injection variability in delivered volumes, and/or require complete replacement of microneedles (e.g., in the middle

Correspondence: Sunandita Sarker (sunandita.sarker@umass.edu) or Ryan D. Sochol (rsochol@umd.edu)
[1]Department of Mechanical Engineering, University of Maryland, College Park, MD 20742, USA
[2]Maryland Robotics Center, University of Maryland, College Park, MD 20742, USA
Full list of author information is available at the end of the article
These authors contributed equally: Sunandita Sarker, Ziteng Wen
Invited Paper for "Microsystems & Nanoengineering/Springer Nature Outstanding Paper Award Winner".

of experimental runs)[17–21]. Such clogging-associated deficits not only diminish scientific and procedural rigor, reproducibility, and productivity, but can also have devastating consequences for applications involving time-sensitive, high-value, and/or supply-limited delivery substances and biological targets[22–27]. Thus, strategies for facilitating novel microneedle architectures that mitigate clogging-induced failure modes are in critical demand.

The predominant approach by which hollow microneedles are manufactured involves four main steps: (i) a cylindrical glass capillary is heated to its material softening point; (ii) the capillary is subjected to tensile axial loading by pulling on the ends to achieve a desired tapered shape; (iii) the capillary is cooled (i.e., to solidify the glass with the intended shape), and then (iv) the tapered tip is opened at a particular location (e.g., by cutting, milling, grinding, or fracturing) to resolve a tip with a target inner diameter (ID) and outer diameter (OD) (Supplementary Fig. S1)[28–33]. Consequently, the standard architectures of hollow microneedles—i.e., with a single opening at the top of the tip—are rooted in these pulling-and-opening manufacturing routines rather than in consideration of clogging susceptibility. Furthermore, with regard to microneedle clogging for such needles, there is an inherent trade-off associated with the size of the tip opening as larger IDs decrease the likelihood of clogging, yet greatly increase the potential of unintentionally damaging or compromising the injection target (e.g., rupturing an embryo, reducing cell viability)[34–36]. It is important to note that in many laboratory and research settings, the tip opening step is completed through manual methods (e.g., breaking the needle tip "by hand" using forceps or small glass shards)—stochastic processes that can lead to irregularities in the size and shape of the needle tip that, in turn, further increase the potential for both clogging as well as needle-induced injury to the injection target[36–40]. One pathway to overcome this clogging-injury trade-off is founded on the use of conventional microfabrication approaches, which researchers have harnessed to achieve hollow microneedles that instead comprise openings orthogonal to the insertion direction to reduce clogging susceptibility[41–47]. Despite the distinctive promise of "side-port" microneedle architectures in remediating undesired tip clogging phenomena, the exceedingly time-, cost-, and labor-intensive microfabrication protocols devised to produce such geometrically complex needles (e.g., via clean room-based silicon micromachining) provide a basis for their extremely scarce adoption by the microinjection community over the past several decades, suggesting a pressing need for alternative manufacturing strategies[48–51].

Additive manufacturing—also referred to as "three-dimensional (3D) printing"—approaches are well established as uniquely suited for achieving sophisticated architectures that would be difficult or infeasible to fabricate using conventional manufacturing methods[52–55]. In the context of applications such as embryo microinjections that require, for example, needles with heights taller than 500 µm (e.g., to reach the yolk) yet diameters on the order of 15 µm (e.g., to prevent embryo rupture)[56–58], the majority of 3D printing techniques lack the resolution and precision needed to additively manufacture such high-aspect-ratio hollow microneedles[59–63]. In contrast, the additive manufacturing approach, "Two-Photon Direct Laser Writing (DLW)", enables 3D architectures to be printed with feature resolutions down to the 100 nm range by scanning a pulsed infrared (IR) laser within a photosensitive material to initiate two-photon polymerization (2PP) at designated locations[64–66]. One hurdle for using DLW to fabricate hollow microneedles, however, is that it is inefficient to scan a micron-to-submicron-sized volume element (i.e., "voxel") point by point to print larger-scale fluidic components that can be manipulated by hand, such as the bulk capillary used to facilitate fluidic loading into the microneedle tip[67–69]. Although researchers have demonstrated that DLW-printed fluidic components, including hollow needle tips, can be manually interfaced with capillaries (e.g., "by hand" using adhesives)[70–73], recent "ex situ DLW (*es*DLW)" approaches allow for 3D microfluidic systems to be printed directly atop—and notably, fully fluidically sealed to—meso/macroscale fluidic components[74–78].

Here, we investigate the potential for *es*DLW-based 3D printing to provide a unique means for fabricating hollow microinjection needles with monolithic 3D architectures that comprise micro/nanostructured features capable of addressing clogging phenomena via two modalities: (i) by using a side-port scheme in which the singular opening at the top of conventional microneedles is replaced with a solid, fine-point tip and, instead, multiple side openings are arrayed fully perpendicular to the direction of penetration, clog-promoting material (e.g., from the injection target) would have to flow in a myriad of indirect directions and become lodged in every single side port to completely block delivery; and (ii) by integrating a 3D microfilter as part of the DLW-printed design, potential debris, aggregates, or other artifacts that could cause back-end needle clogging during microinjections[79–81] are physically prevented from entering the thin, internal microchannel of the needle tip (Fig. 1). In addition, the reliance on DLW provides an array of design and manufacturing benefits compared to alternative fabrication strategies. In contrast to conventional microfabrication approaches, which suffer from poor control over microneedle geometry—e.g., resulting in rectangular design motifs, low needle aspect ratios, and/or challenges in positioning the outlet port(s)[41–46]—DLW enables unparalleled submicron-scale geometric versatility to resolve

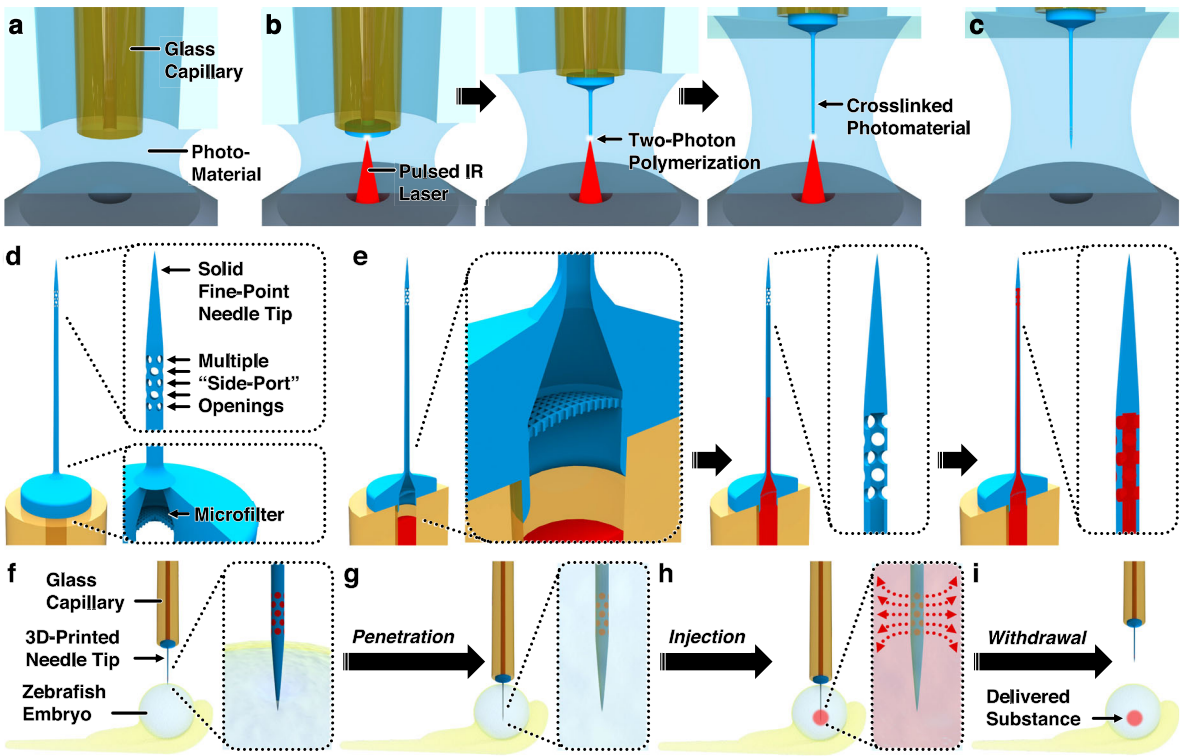

Fig. 1 Conceptual overview of using "ex situ Direct Laser Writing (*es*DLW)" to additively manufacture hollow microneedles with 3D architectures for embryo microinjections. a–c The *es*DLW strategy for printing the monolithic 3D microneedle tip. **a** A glass capillary—e.g., an amber-fused silica tube—loaded into a DLW 3D printer with one end enveloped in photosensitive material. **b** A tightly focused femtosecond infrared (IR) laser is scanned point by point, layer by layer within the photosensitive material to initiate two-photon polymerization (2PP) in designated locations directly atop the capillary. **c** The completed needle tip fluidically sealed to the capillary. **d** Key DLW-enabled 3D architectural needle tip features. **e** The microfluidic loading and delivery path in which a fluid/suspension passes: (*left*) from the capillary into the printed needle tip through the internal microfilter, (*middle*) through the thin main channel, and then (*right*) out of the tip via multiple "side-port" openings (i.e., perpendicular to the main channel). **f–i** Key steps for zebrafish embryo microinjections. **f** The solid, fine-point tip puncturing the surface of the embryo. **g** The microneedle penetrating into the embryo. **h** Microinjection-based delivery of foreign substances into the embryo via the microneedle tip's multiple side-port openings. **i** Withdrawal of the microneedle from the embryo, leaving behind the delivered substance

hollow microneedles with high aspect ratios (e.g., 15 µm ODs, 10 µm IDs, and >500 µm heights), curvilinear topologies, integrated microfilters, and customizable shapes, tip sharpness, and positioning of outlet port(s). Furthermore, the streamlined, rapid (i.e., ≤10 min), 3D printing process, which involves minimal manual labor, not only bypasses the deficits of traditional cleanroom microfabrication approaches (e.g., complex, time-consuming, expensive, and/or laborious multi-step protocols)[48–51], but also affords a level of design control that obviates the need for time-, cost-, and labor-intensive post-processing routines (e.g., fire polishing and focused ion beam polishing) used to further refine needle-tip architectures[82–85]. Through serial microinjection experiments performed using live zebrafish embryos, we evaluate the anti-clogging capabilities of the novel 3D microneedle architecture compared to both conventional laboratory glass-pulled microneedles as well as *es*DLW-printed control microneedles designed to resemble conventional needles. We find that the 3D microneedles with multiple side openings not only limit the undesired high variability in delivered volumes associated with both control needles but also fully prevent the occurrence of complete clogging failures (i.e., cases in which no volume is delivered via the microneedle). In combination, the reported *es*DLW-enabled 3D hollow microneedle design and additive manufacturing strategy offers a promising route to overcome pervasive clogging-associated obstacles to microinjection efficacy, thereby holding unique potential for biomedical applications that span from laboratory research settings to the clinic.

Results

Design and *es*DLW-based additive manufacturing of 3D hollow microneedles

A conceptual overview of the *es*DLW protocol for additively manufacturing 3D hollow microneedle architectures with anti-clogging features is presented in Fig.

1a–c. Initially, a glass capillary (e.g., an amber fused silica capillary) is loaded into a DLW 3D printer with photosensitive material encompassing the capillary base (Fig. 1a). Next, a tightly focused femtosecond IR laser is scanned in a point by point, layer by layer manner to photopolymerize the hollow microneedle tip structure directly onto the glass capillary (Fig. 1b). Following completion of the *es*DLW 3D printing process (Fig. 1c), the microneedle-capillary assembly is removed from the printer and developed for subsequent use.

The resulting needle tip—printed as a single, monolithic piece—includes three architectural changes from conventional microinjection needles (Fig. 1d). First, the top of the microneedle includes a sealed (i.e., solid) fine-point tip. Correspondingly, directly below the fine-point tip, the needle is arrayed with multiple side-port openings. Lastly, the base of the printed needle includes a microporous filter structure adjacent to the glass capillary (Fig. 1d). These geometric changes to the microneedle design offer a means to address several modes that contribute to undesired clogging phenomena and failures during microinjections. In particular, because fluids and/or suspensions must first pass through the printed microfilter before entering the thin main channel of the microneedle tip and then exiting out the multiple side ports (Fig. 1e), potential particulates that could clog the channel or side-port openings are blocked by the filter, thereby preventing such issues from manifesting. During injection protocols, such as zebrafish embryo microinjections, unlike conventional needles with a single opening at the top of the tip, material from the injection target is unable to enter—and, in turn, clog—the solid, fine-point tip as it punctures and penetrates into the target (Fig. 1f, g). Such penetration-associated clogging failures would instead require material from the target to flow in various directions orthogonal to the insertion direction to become lodged in every single side port. Contingent upon any portion of side ports remaining functional following penetration, fluids or suspensions can be delivered into the target (Fig. 1h), and the microneedle can be withdrawn for subsequent microinjections with additional targets (Fig. 1i).

In this study, we investigated 3D microneedles for use in serial zebrafish microinjection protocols as an exemplar. To maintain consistency with dimensions of conventional laboratory glass-pulled microneedles used for such protocols (e.g., Supplementary Fig. S1), we designed the 3D microneedle tip with a height of 650 μm, an OD of 15 μm (tapered from 20 μm at the base), and an ID of 10 μm (Supplementary Fig. S2). It is important to note that we designed the placement and size of the side-port openings with respect to DLW-specific manufacturing considerations—namely, the size and ovular shape of the 2PP voxel—which allows for smaller features to be resolved perpendicular to the tip compared to those in the parallel direction for the presented print orientation. Accordingly, the voxel's size and shape also dictate the maximum number of side ports that can be integrated within a certain region. For the DLW configuration used in this work, the voxel size includes a lateral (*x-y*) dimension of 0.6 μm and a vertical (*z*) dimension of 3.3 μm[86], which allows for 20 arrayed side ports (Supplementary Fig. S2) that each can be designed to ultimately resolve 5-μm-diameter orifices as reported previously[87,88]. In addition, we designed a control microneedle with the same ID and OD as the 3D microneedle, but with a single, 30°-tapered opening located at the top of the tip (Supplementary Fig. S3) that resembles conventional needles to, in turn, allow for decoupled experimental comparisons in which tip geometry (i.e., a single 10-μm-in-diameter top port versus multiple side ports) is the only variable. Importantly, we designed both the 3D and control microneedles to include an integrated curvilinear microfilter—with arrays of 3.5 μm × 3.5 μm micropores—in the base as well as curvilinear and gradually tapered internal features extending from the base to the needle tip to minimize dead volumes during microinjections (Supplementary Fig. S2; Supplementary Fig. S3). Furthermore, to prevent dead volumes at the top of the 3D microneedle, we designed the bottom of the solid, fine-point tip to be tangent to the top-most side-port openings (Supplementary Fig. S2).

We printed both sets of microneedles using the commercially available photoresist, IP-L (Nanoscribe GmbH & Co. KG, Eggenstein-Leopoldshafen, Germany), directly atop amber fused silica capillaries (ID = 75 μm; OD = 360 μm; Molex LLC, Lisle, IL). For the 3D microneedle design, the *es*DLW printing process was completed in ~10 min (Fig. 2a, b; Supplementary Movie S1). Due to the ovular shape of the print voxel, the side ports resolved with diameters of 5 μm (Fig. 2c). For the control design, the lack of fine details (e.g., associated with the side ports and solid, fine-point tip) allowed for the *es*DLW printing process to be completed in 5 min (Fig. 2d, e; Supplementary Movie S2). Micrographs of the assemblies captured using a low-vacuum scanning electron microscope (SEM) revealed effective alignment and integration of the *es*DLW-printed microneedles with the fused silica capillaries without any visible signs of physical defects along the microneedle base-capillary interface (Fig. 2c, f). In addition, we printed sectioned microneedles to provide visualization of the microfilter structures, which revealed pore sizes of ~3.25 μm × 3.25 μm (Fig. 2g, h). Because these micropores are smaller than the side ports (Fig. 2c), it is unlikely that particulates capable of bypassing the filter would subsequently clog the main channel or the side ports.

We also investigated the fidelity of the *es*DLW printing process for resolving microneedle tips with 15 μm ODs and 10 μm IDs by performing optical measurements from micrographs of both sets of printed microneedles.

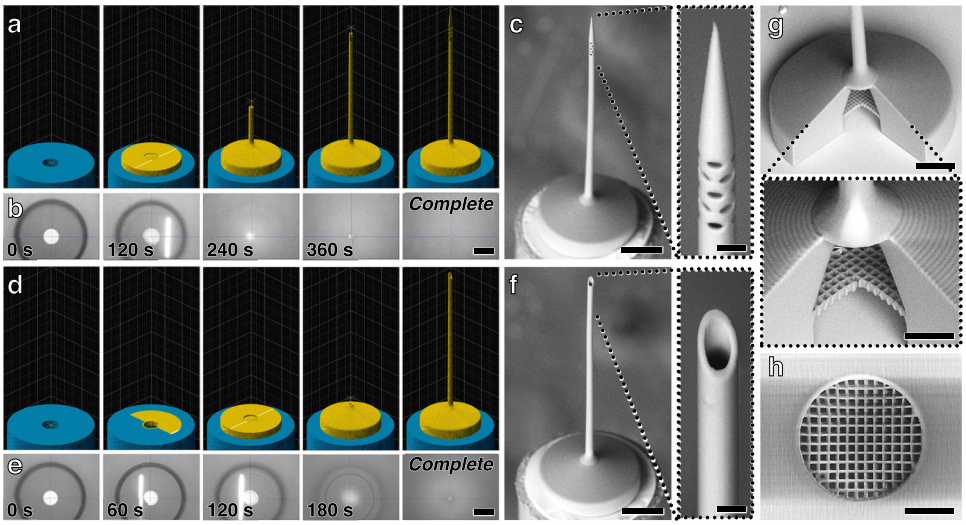

Fig. 2 Fabrication results for *es*DLW-based 3D printing of microinjection needles directly atop fused silica glass capillaries. a–**c** 3D needle tip designs. **d**–**f** Control tip designs. **a, d** Computer-aided manufacturing (CAM) simulations, and **b, e** corresponding micrographs captured during the *es*DLW printing process. Scale bars = 100 µm (*See also* Supplementary Movie S1; Supplementary Movie S2). **c**, **f** Scanning electron microscope (SEM) images of representative printing results. Scale bars = 100 µm (Expanded views = 10 µm). **g**,**h** SEM micrographs of printed integrated microporous filters. **g** Sectioned view. Scale bar = 100 µm (Expanded view = 25 µm). **h** Bottom view. Scale bar = 25 µm

Fabrication results quantified from SEM micrographs revealed mean ODs of 15.3 ± 0.1 µm ($n = 10$) and 15.4 ± 0.2 µm ($n = 10$) for the 3D and control microneedle designs, respectively (Supplementary Fig. S4a). Results quantified from brightfield micrographs revealed mean IDs of 10.3 ± 0.1 µm ($n = 10$) and 10.2 ± 0.2 µm ($n = 10$) for the 3D and control microneedle designs, respectively (Supplementary Fig. S4b). In both cases, the *es*DLW-printed microneedles exhibited substantially lower needle-to-needle variability than that for the standard laboratory glass-pulled microneedles, which revealed a mean tip OD and ID of 15.0 ± 4.0 µm and 9.50 ± 3.1 µm, respectively (Supplementary Fig. S4). This order-of-magnitude improvement in needle-to-needle repeatability suggests that, beyond affording the ability to resolve unique 3D microneedle designs, the *es*DLW strategy could also provide a pathway to obviate the need for the time-intensive needle-specific calibration protocols typically required for such standard laboratory needles.

Microfluidic interrogations of microneedle-capillary interface integrity in vitro

Consistent with previous reports for *es*DLW-based technologies, the successful adherence of the DLW-printed structure to the meso/macroscale component on which it is printed is critical to performance efficacy[74–78,89–91]. For the application of fluidic microinjections specifically, the potential consequences of poor interface integrity correspond to the degree of adherence failure. In cases of minor microneedle-capillary detachments, fluid would leak out of the interface—i.e., before entering the printed needle tip—which would not only reduce the volume delivered into the biological target via the designated port(s), but also lead to undesired losses of the fluidic payload. In the case of a major detachment, the printed needle tip could end up remaining lodged in the delivery target (e.g., inside an embryo).

To investigate the potential for both of these failure modes, and, in turn, provide insight into the mechano-fluidic integrity of the interface between the *es*DLW-printed microneedle tips and the fused silica glass capillaries on which they were printed, we performed two sets of microfluidic burst-pressure experiments for the control and 3D needle tip designs with respect to the 35 kPa pressure input required for the exemplar, zebrafish embryo injections. First, we performed linear burst-pressure tests in which an aqueous fluid was infused into the microneedles as the input pressure was increased from 0 to 200 kPa at a rate of 1 kPa/s while observing the microneedle-capillary interface under brightfield microscopy and monitoring the flow rate through the system. Throughout testing for ten distinct microneedle-capillary assemblies per tip design ($N = 20$ assemblies in total), we did not observe any visible signs of undesired leakage out of the interface, with fluid exiting solely via the top port(s) (e.g., Fig. 3a, b). Quantified results for the flow rate versus input pressure relationships corroborated this interface integrity behavior (Fig. 3c, d). Potential interface failures (i.e., detachments of the base of the DLW-printed microneedle tip from the capillary) during linear burst-pressure testing would manifest in the data in one of two

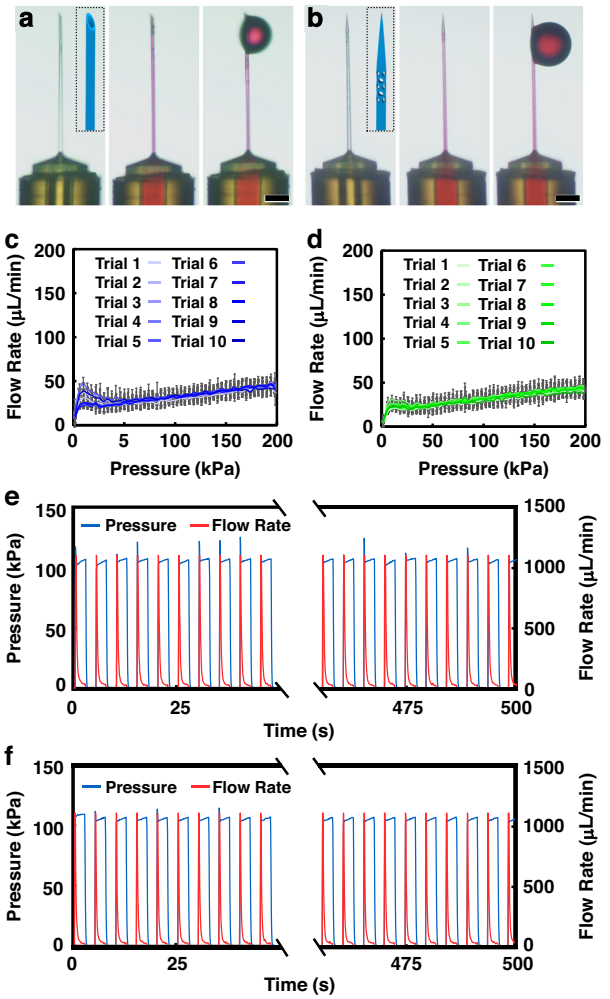

Fig. 3 Experimental results for microfluidic investigations of print-capillary interface integrity. a,**b** Sequential images of fluidic infusion of rhodamine-dyed DI water into *es*DLW-printed microinjection needles with **a** control, and **b** 3D needle tip designs. Scale bars = 100 µm. **c**,**d** Linear microfluidic burst-pressure results for *es*DLW-printed microinjection needles with **c** control, and **d** 3D needle tip designs ($n = 10$ distinct needles per design). Error bars = S.D. **e**,**f** Representative cyclic microfluidic burst-pressure results for $n = 100$ ramping cycles for *es*DLW-printed microinjection needles with **e** control, and **f** 3D needle tip designs

modes. In cases with minor detachments, because the flow rate is linearly related to the input pressure by:

$$Q = \frac{\Delta P}{R_H} \tag{1}$$

where Q is the flow rate, ΔP is the pressure difference, and R_H is the hydraulic resistance, the unintended emergence of leakage pathways through the interface will lead to reductions in R_H with corresponding increases in the slope of the flow rate versus pressure curve. In the case of a major detachment (i.e., a burst event), R_H would decrease substantially, resulting in an instantaneous, dramatic increase in the flow rate. Quantified experimental results for both microneedle tip designs did not reveal any such phenomena, instead exhibiting smooth, consistent flow rate versus input pressure behavior (Fig. 3c, d). One caveat to these data is that the burst-pressure experiments were initiated with empty microneedle-capillary assemblies, which led to some irregularities in flow rate trends at lower pressures—particularly for the control tip design case—as air (e.g., bubbles) initially evacuated from the system in response to the applied pressures. Nonetheless, these linear burst-pressure results suggest that the microneedle-capillary interface for both the control and 3D tip designs can withstand input pressures of up to 200 kPa.

While a variety of microinjection applications (e.g., in clinical settings) rely on a single injection performed with a single-use microneedle, many use cases in research settings involve serial microinjections in which a single microneedle is used to perform high numbers of injections. Thus, to examine the microneedle-capillary interface integrity under such mechanofluidic loading scenarios, we conducted a second set of studies in which input pressures in excess of 100 kPa were applied repeatedly. Akin to the linear burst-pressure tests, we monitored the microneedle-capillary interface optically as well as the flow rate through the system while an aqueous fluid was infused into the microneedles; however, for the cyclic burst-pressure tests, the input pressure was repeatedly applied at ≥100 kPa for 2.5 s and then at 0 kPa for 2.5 s for $n = 100$ cycles. In this case, a burst event would be evident by the flow rate remaining at a high magnitude throughout the duration of the applied pressure. Quantified experimental results from the cyclic microfluidic burst-pressure experiments for both the control and 3D needle tip designs did not indicate any signs of such burst behavior (e.g., Fig. 3e, f). In contrast, apart from initial artifacts from the rapid onset of applied pressure, the data revealed that the flow rates quickly returned to magnitudes on the order of those found during the linear burst-pressure tests (Fig. 3c–f). Visual examinations performed throughout these studies under brightfield microscopy corroborated these results as we did not observe any indications of leakage or catastrophic burst along the microneedle-capillary interface for ten different microneedle-capillary assemblies corresponding to each tip design ($N = 20$ assemblies in total). Furthermore, we did not observe any significant differences in flow rate (i.e., fluidic delivery) performance between the printed microneedles with the control and 3D tip designs in either the linear (Fig. 3c, d) or cyclic (Fig. 3e, f) burst-pressure studies, indicating that not only did both sets of printed microneedles retain consistent print-capillary interface integrity, but that the differences in tip design also did not appear to affect the baseline fluidic delivery

profiles. In combination, these results suggest that the presented *es*DLW-based microneedle fabrication strategy is suitable for both single-use and serial microinjection scenarios corresponding to input pressures of 200 kPa and 100 kPa, respectively, as well as for both of the tip designs examined.

3D microneedle-mediated delivery of fluorescent material into live zebrafish embryos in vivo

As an exemplar with which to elucidate the microinjection efficacy of the *es*DLW-printed microneedles, we performed experiments in which single microneedles were each used to perform 100 serial injections of a fluorescently labeled aqueous fluid—in this case, rhodamine B-dyed DI water—into live, manually dechorionated zebrafish embryos (wildtype AB genotype) in vivo (e.g., Fig. 4a–d). We conducted experiments with three sets of microneedles: (i) conventional laboratory glass-pulled microneedles, (ii) *es*DLW-printed microneedles with the control tip design, and (iii) *es*DLW-printed microneedles with the 3D tip design. For each type of microneedle, we performed trials using ten different needles that each entailed 100 serial microinjections (i.e., $n = 1000$ injections per needle type; $N = 3000$ injections in total). Following each set of 20 microinjections, we lysed the corresponding embryos separately and then loaded the lysates into a plate reader for fluorescence intensity measurements as a means to quantify the volume of fluorescently labeled aqueous fluid delivered into (and retained in) the embryos. Quantified results revealed that while the mean fluorescence intensities associated with the conventional glass needles and the *es*DLW-printed control microneedles were not statistically distinguishable, the mean fluorescence intensities for the *es*DLW-printed microneedles with the 3D tip design were consistently higher than those of both the conventional glass and printed control needles (Fig. 4e). This difference was most pronounced for the first 20 microinjections with a mean fluorescence intensity of 9.41 ± 1.87 for the 3D microneedles compared to 4.52 ± 1.58 for the conventional glass needles ($p < 0.0001$) and 5.73 ± 1.38 for the *es*DLW-printed control needles ($p < 0.001$); however, even in this case, the conventional glass and printed control needles were not statistically distinguishable ($p = 0.10$). For the microinjection groups from 21 to 100 injections, the fluorescence measurements appeared consistent from group to group. For example, results for microinjection groups 21–40 and 81–100 included 4.09 ± 1.06 and 3.75 ± 1.56 for the conventional glass needles ($p = 0.60$), 4.59 ± 1.02 and 4.67 ± 0.96 for the *es*DLW-printed control needles ($p = 0.87$), and 7.34 ± 1.58 and 7.16 ± 1.30 for the *es*DLW-printed 3D microneedles ($p = 0.79$), respectively, with the 3D microneedle exhibiting higher intensities in all cases (Fig. 4e).

Although these quantified fluorescence intensity data are in agreement with the hypothesis that the 3D microneedle architecture would prevent microinjection-associated clogging failure modes and, in turn, yield improvements in delivery efficacy, there are several additional factors that could also contribute to these results. The fluorescence results are based not only on the volume of material initially delivered into the embryo during the microinjection step, but also on the capacity for the embryo to retain the delivered material during and following withdrawal of the microneedle. Compared to the tips of the standard glass-pulled laboratory needles (e.g., Supplementary Fig. S1b, c), it is possible that the improved consistency and sharpness of the printed microneedle profiles (Fig. 2c, f; Supplementary Fig. S4) could facilitate smoother puncture, penetration, and/or withdrawal operations—with the added potential that the fine-point geometry of the 3D needle tip design could also prevent unintended coring of the embryo (i.e., where a small, cylindrical section of the embryo is removed during penetration). Either independently or in combination, these factors would contribute to enhanced post-injection retention efficacy of the embryos (and higher fluorescence intensities). It is important to note that such capabilities are desirable for microinjection applications and could offer the potential to limit microneedle-associated injury to injection targets (e.g., to improve post-injection embryo viability). Although we did not directly investigate post-injection delivery losses (e.g., leakage) or assess post-injection embryo viability in the current study, micrographs of post-injection embryo batches did reveal indications that the conventional glass-pulled laboratory microneedles appeared to lead to more post-injection embryo fragments compared to both *es*DLW-printed microneedles (Supplementary Fig. S7). Nonetheless, within the context of the fluorescence results specifically, these possibilities suggest that the enhanced fluorescence intensities for the *es*DLW-printed microneedles with the 3D tip design cannot be attributed solely to anti-clogging functionalities.

Investigations of microneedle clogging associated with serial microinjections into live zebrafish embryos in vivo

To elucidate injection performance metrics and failure modes linked directly to microneedle clogging, we performed pseudo-injections before and after each set of 20 microinjections over the course of 100 serial injection runs with zebrafish embryos. Specifically, these experiments—conducted with conventional laboratory glass-pulled microneedles, *es*DLW-printed microneedles with the control tip design, and *es*DLW-printed microneedles with the 3D tip design—entailed three main steps: (i) prior to the first microinjection into an embryo with a microneedle, we carried out five pseudo-injections of the

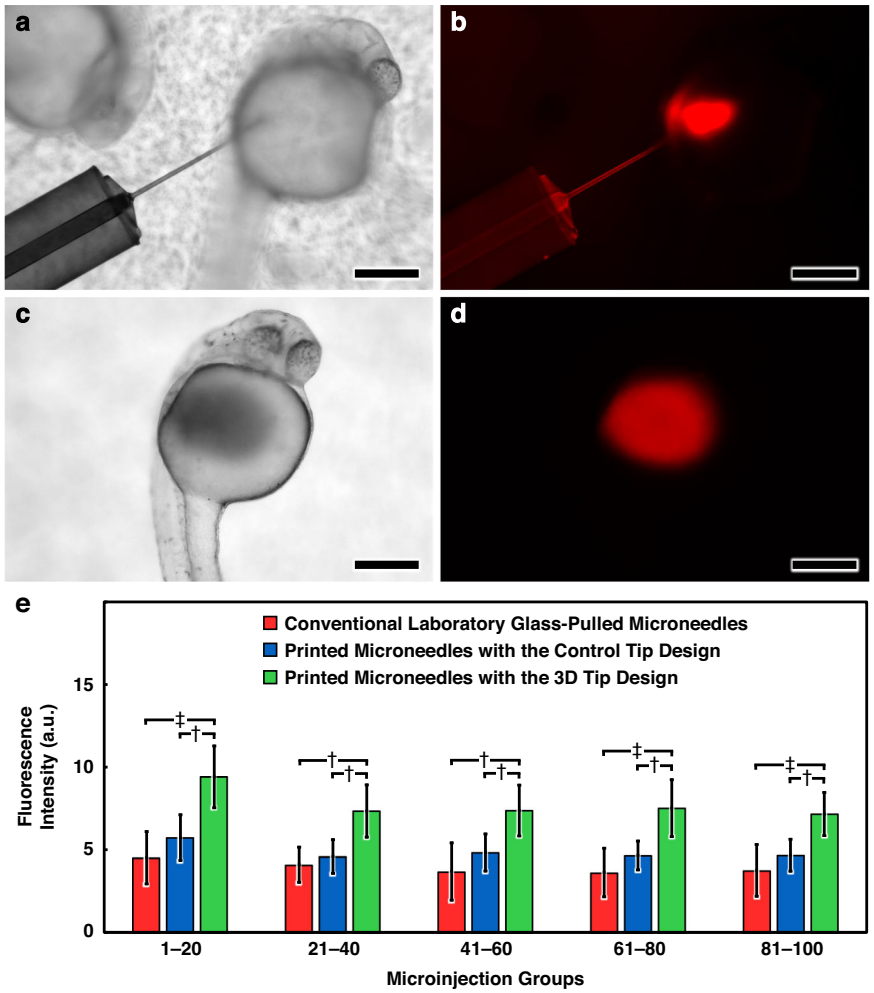

Fig. 4 Experimental results for microinjections of fluorescently labeled aqueous fluid into live dechorionated zebrafish embryos in vivo. **a**–**d** Sequential micrographs **a**, **b** during, and **c**, **d** after delivery of rhodamine B-dyed DI water into an embryo using an *es*DLW-printed microneedle with a 3D tip design imaged under **a**, **c** brightfield, and **b**, **d** fluorescence microscopy. Scale bars = 250 µm. **e** Quantified fluorescence intensity of groups of lysed zebrafish embryos following microinjection with various needle types ($n = 10$ distinct microneedles per needle type with 100 microinjections per needle; $N = 3000$ microinjections in total). Error bars = S.D.; † and ‡ denote $p < 0.001$ and $p < 0.0001$ statistical significance, respectively

aqueous fluid (rhodamine B-dyed DI water) into a droplet of oil on a microscope calibration slide (e.g., Supplementary Fig. S5), thereby providing a means to measure the initial delivery volumes based on the sizes of the delivered aliquots; (ii) we used the microneedle to perform 20 microinjections with live, manually dechorionated zebrafish embryos in vivo (e.g., Fig. 5a); and then (iii) we carried out a single pseudo-injection of the aqueous fluid into a droplet of oil on a microscope calibration slide to allow for measurements of the delivered volumes following embryo microinjections and, in turn, capture potential changes in injection volume and clogging effects. The second and third steps were repeated (i.e., at 20-injection increments) until completion of the 100 serial injections, resulting in six sets of volume measurements per needle trial ($n = 10$ pseudo-injection aliquots per needle) with ten distinct microneedles per needle type (i.e., $n = 100$ pseudo-injection aliquots per needle type; $N = 300$ pseudo-injection aliquots in total).

To account for potential differences from needle to needle, for each microneedle, we normalized the injection volumes measured following zebrafish embryo injections with respect to the mean of the initial injection volumes (i.e., from $n = 5$ pseudo-injection aliquots before the first embryo microinjection). In addition, we monitored all instances of complete clogging in which pseudo-injection attempts were unsuccessful—i.e., cases in which the microneedle obstructed to the degree that no fluid volume could be delivered.

Quantified experimental results for the normalized delivery volumes revealed three key trends (Fig. 5b–d). First, we observed many cases in which microneedles

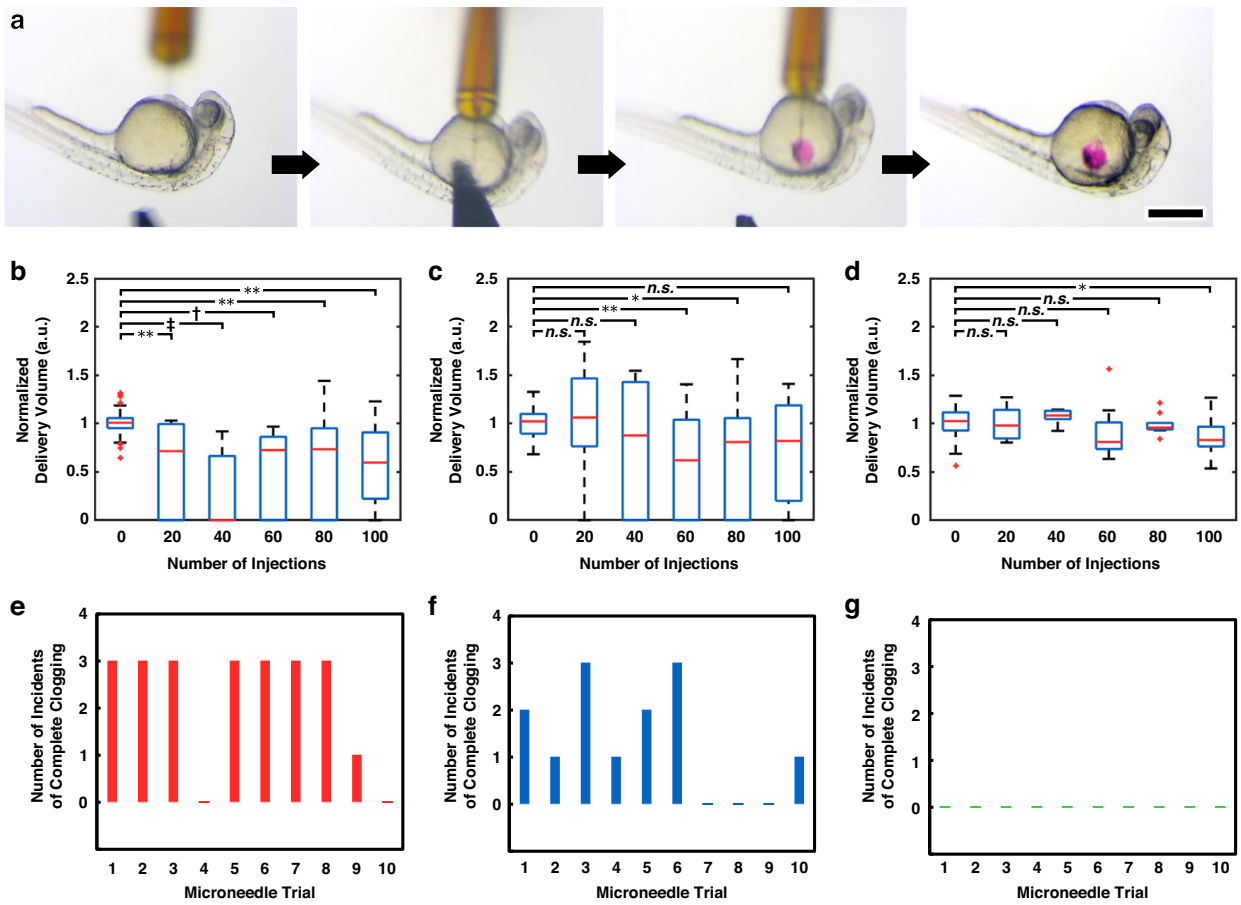

Fig. 5 Experimental results for clogging phenomena associated with microinjections into live dechorionated zebrafish embryos for various microneedle types. a Sequential micrographs of the embryo microinjection process using an *es*DLW-printed microneedle with a 3D tip design. Scale bar = 500 µm; *See also* Supplementary Movie S3. **b**–**d** Normalized delivery volumes measured at 20-injection increments over the course of serial injection trials comprising 100 zebrafish embryo microinjections for: **b** conventional laboratory glass-pulled microneedles, **c** *es*DLW-printed microneedles with the control tip design, and **d** *es*DLW-printed microneedles with the 3D tip design ($n = 10$ distinct microneedles per needle type). *, **, †, and ‡ denote $p < 0.05$, 0.01, 0.001, and 0.0001 statistical significance, respectively; n.s. = not significant. **e**–**g** Number of incidents of complete microneedle clogging (i.e., cases in which no fluid was delivered during a pseudo-injection attempt) per trial examined at 20-injection increments ($n = 5$ delivery volume assessments per trial) over the course of serial injection trials comprising 100 microinjections for: **e** conventional laboratory glass-pulled microneedles, **f** *es*DLW-printed microneedles with the control tip design, and **g** *es*DLW-printed microneedles with the 3D tip design ($n = 1$ distinct microneedle per trial; 10 distinct microneedles per needle type)

exhibited clogging-associated behaviors during earlier pseudo-injection assessments (e.g., after 40 or 60 injections) followed by improved volume delivery in later assessments (e.g., after 80 or 100 injections)—particularly for the conventional glass and printed control needles (Fig. 5b, c)—suggesting that microneedle clogging was both variable and impermanent (i.e., clogged needles could become unclogged) during the course of the serial microinjections. Second, the conventional laboratory glass-pulled needles were the only microneedles examined for which the pseudo-injection delivery volumes were significantly lower in every case following the onset of embryo microinjections, with normalized volumes ranging from 0.58 ± 0.51 ($p < 0.005$) following 80 injections down to 0.30 ± 0.37 ($p < 0.0001$) following 40 injections (Fig. 5b). In contrast, results for the *es*DLW-printed microneedles with the control tip design revealed only two cases of significant reductions in delivery volume, with normalized volumes of 0.68 ± 0.55 ($p < 0.01$) and 0.75 ± 0.56 ($p < 0.05$) following 60 and 80 injections, respectively (Fig. 5c), while for the *es*DLW-printed microneedles with the 3D tip design, only the final case (i.e., following all 100 injections) with a normalized delivery volume of 0.85 ± 0.20 was statistically discernible ($p < 0.05$) from the initial delivery volumes (Fig. 5d). Lastly, the variability in the normalized delivery volumes was markedly higher for both the conventional laboratory glass-pulled needles and *es*DLW-printed microneedles with the control tip design compared to the *es*DLW-printed microneedles with the 3D tip design (Fig. 5b–d).

For example, the magnitudes of the standard deviation (S.D.) for the normalized delivery volumes corresponding to the conventional glass microneedles ranged from 0.37 to 0.51, while those for the *es*DLW-printed 3D microneedles ranged from 0.07 to 0.26.

Quantified results for the number of instances of complete microneedle clogging observed during the pseudo-injection delivery assessments (Fig. 5e–g) suggest that such failure modes contributed to the high delivery variability associated with the conventional glass and printed control needle cases (Fig. 5b–d). Among the ten conventional laboratory glass-pulled microneedles tested, seven needles exhibited complete clogs in three out of the five assessments, with an overall complete clogging rate of 44.0 ± 26.3% (Fig. 5e). The *es*DLW-printed microneedles with the control tip design revealed an average complete clogging rate of 26.0 ± 23.2%, which, while not statistically discernible from the conventional glass case ($p = 0.12$), included only two needles with complete clogs in three out of the five pseudo-injection assessments (Fig. 5f). In contrast to the conventional glass and printed control needle cases—with two and three microneedles not exhibiting any complete clogging events, respectively (Fig. 5e, f)—experiments with the *es*DLW-printed microneedles with the 3D tip design did not reveal any instances of complete clogging throughout all of the pseudo-injection delivery assessments (Fig. 5g).

With regard to the *es*DLW-printed microneedles specifically, these results differ from those of the in vitro microfluidic cyclic burst-pressure experiments, which did not reveal indications of differences in delivery performance between the control and 3D tip designs (Fig. 3c–f). For the in vivo experiments in which the microneedles repeatedly penetrated into the zebrafish embryos, however, only the control design exhibited high delivery variability and frequent complete clogging events in which applied pressure failed to deliver fluid through the microneedle (Fig. 5c, d, f, g). In combination, these results suggest that while integrating a 3D microfilter as part of the needle tip design—as was the case for both the control and 3D *es*DLW-printed microneedles—can help to mitigate clogging phenomena to a degree (in the context of aqueous fluidic payloads), rearchitecting the needle tip geometry from the single top opening configuration of conventional needles to the presented 3D side-port scheme offers a unique means to address undesired clogging phenomena and enhance the consistency of microneedle-mediated delivery.

Discussion

In this work, we investigated the potential of using submicron-scale additive manufacturing as a strategy for fabricating high-aspect-ratio, hollow microneedles with 3D tip architectures designed to address multiple modes of microneedle clogging phenomena, which we evaluated via serial microinjections of zebrafish embryos in vivo. From a microfabrication standpoint, the presented *es*DLW approach allowed for the geometrically sophisticated microneedle tip architectures—featuring a solid, fine-point tip, multiple 5-μm-in-diameter side ports, and an integrated microfilter with 3.25 μm × 3.25 μm pores—to be 3D microprinted directly atop mesoscale glass capillaries without the need for sealants/adhesives, yet demonstrated the ability to withstand cyclic and linear pressure loading in excess of 100 kPa and 200 kPa, respectively. These capabilities could be extended not only to a broader range of hollow microneedle-based applications, such as for drug delivery scenarios[92–95], but also to advance integrated membrane and microfiltration capabilities in lab-on-a-chip systems[96–98]. In addition, the microneedles in this study included heights of 650 μm, tip ODs of 15 μm, and IDs of 10 μm, which represent the highest aspect ratios (~40) for *es*DLW-printed structures reported in the literature and, thus, could have important implications for *es*DLW-enabled technologies that benefit from high-aspect-ratio architectures, such as microsurgical instruments[99–101]. Although we did not find the 5- and 10-min print times for the control and 3D needle tip designs, respectively, to be prohibitive, it is important to note that recent advances for DLW-based 3D printing—namely, the higher laser powers, faster scan speeds, and dynamic optical tuning capabilities (e.g., adaptive resolution printing and voxel tuning) of current commercially available DLW 3D printers[102]—as well as alternative ultrahigh-printing-speed photoresists[103] offer the potential to reduce these microneedle print times dramatically. Furthermore, in contrast to conventional laboratory glass-pulled microneedles that often require arduous calibration routines due to undesired needle-to-needle variability, the characterization results suggest that such calibration protocols may not be necessary for microneedles produced using DLW as the needle-to-needle precision in critical dimensions (e.g., ID and OD) for the printed microneedles was notably higher than that for the conventional glass needles (Supplementary Fig. S4).

Within the context of biological microinjection applications, the serial zebrafish embryo injection studies illustrate the utility of the 3D microneedle architecture in curbing clogging failure phenomena. Comparisons of fluidic delivery performance between the conventional laboratory glass-pulled microneedles and the *es*DLW-printed microneedles with the control design—which both include similar tip geometries with a single top port, but only the printed microneedle comprises an internal microfilter—suggest that the integrated microfilter can aid in reducing clogging phenomena to a degree; however, the results for the 3D tip design indicated that the side-port modifications are critical for effectively addressing microneedle clogging. It is important to note that, as the payload in this study was an aqueous liquid, it is possible

that the integrated filters could provide more apparent benefits for microinjection applications that rely instead on fluidic suspensions. Nonetheless, as the only needle type examined that did not reveal any cases of complete needle clogging throughout the zebrafish embryo microinjection investigations, the *es*DLW-printed microneedles with the 3D tip design hold distinctive promise for broad microinjection protocols that can be negatively affected by instances of microneedle clogging. Accordingly, the 3D microneedles in this study could offer a powerful means to enhance injection efficiencies, reduce undesired needle-to-needle and injection-to-injection variability in delivered volumes, and/or prevent the need for premature replacements of microneedles during experimentation, thereby providing a new pathway to enhance the scientific and procedural rigor, reproducibility, and productivity associated with applications founded on microneedle-mediated microinjections.

Beyond exploring these potential capabilities enabled by addressing clogging-associated failure modes, the fluorescence microinjection results and micrographs of post-injection embryos (Supplementary Fig. S7) suggest that future efforts should also focus on investigating the possibility that the rearchitected 3D microneedle geometry—namely, the solid, fine-point tip—could potentially mitigate failure modes stemming from needle-induced injury to biological targets during puncture, penetration, and retrieval operations. Furthermore, while the current study centered on zebrafish embryos as an exemplar with regard to their importance as a model in scientific research, the 3D microneedles could be adapted to facilitate microinjections for a wide range of biological targets (e.g., cells, embryos, tissues, organs, and organisms) and delivery substances (e.g., cells, DNA, RNA, proteins, viruses, and micro/nanoparticles), with particular utility for cases involving serial microinjections and/or high-value samples. Consequently, given the fundamental role of microinjection technologies in fields ranging from genetic engineering and biomedical science to pharmacology and reproductive medicine, the presented DLW-enabled 3D microneedle strategy and foundational findings could have far-reaching implications across laboratory research and clinical applications.

Methods

Microneedle fabrication via *es*DLW-based additive manufacturing

The models for the microneedles with the 3D and control designs were both generated using the computer-aided design (CAD) software, SolidWorks (Dassault Systèmes, France) (Supplementary Figs. S2, S3). The models were exported as STL files and then imported to the computer-aided manufacturing (CAM) software, DeScribe (Nanoscribe GmbH & Co. KG, Eggenstein-Leopoldshafen, Germany), to define the laser writing path and parameters for the Nanoscribe Photonic Professional GT2 DLW 3D printer. Prior to the printing process, fused amber silica polyimide-coated smooth solid tubes (Molex LLC, Lisle, IL) with IDs of 75 µm and ODs of 360 µm were cut to ~2 cm in length using a fused silica capillary cutter (Postnova Analytics Inc., Salt Lake City, UT). To improve adhesion between the base of the printed microneedle and the top surface of the capillary, the capillary tubes were silanized before printing via: (i) sequential rinses with acetone and isopropyl alcohol (IPA), (ii) drying with N_2 gas, (iii) O_2 plasma etching the slide with a power setting of 75 W for 30 min using a Plasma Cleaner (PIE Scientific, Union City, CA), (*iv*) submerging the capillary in a solution comprising 30 ml of ethanol and 150 µl of 3-(trimethoxysily)propyl methacrylate (Sigma-Aldrich, St. Louis, MO) for 2 h, and then (*v*) rinsing the capillary with acetone and IPA was rinsed (followed by drying with N_2 gas). The capillary was mounted into the Nanoscribe DLW printer using a custom holder to promote alignment and a droplet of IP-L photoresist (Nanoscribe) was placed in contact with the designated print surface of the capillary (Supplementary Fig. S6). The microneedles were printed directly onto the capillary by scanning a femtosecond IR laser (scan speed = 0.1 m/s) to polymerize the photoresist with different sets of DLW parameters tailored to each of the three sections of the microneedle—i.e., the base, the needle body, and the needle tip (Supplementary Table S1). Following the DLW printing process, the microneedle-capillary assembly was removed from the printer and developed by immersing the assembly in propylene glycol methyl ether acetate (PGMEA) for 1 h. The opposing end of the capillary (i.e., without any printed structures) was coupled to silicone rubber tubing (#51135K11, McMaster-Carr, Elmhurst, IL) via inner-lok GC union adapters (Moles) and negative pressure (i.e., suction) was applied using a BD Luer-Lok syringe (Becton, Dickinson and Company, Franklin Lakes, NJ) to evacuate residual photoresist and/or developer from the interior of the microneedle-capillary assembly. Lastly, the syringe was loaded with IPA and then used to perfuse IPA through the interior of the microneedle-capillary assembly.

Conventional laboratory glass-pulled microneedles

The glass microcapillary needles used in this study were fabricated from borosilicate glass capillary tubes with an outer diameter of 1.0 mm and an inner diameter of 0.5 mm (Narishige GD-1, Amityville, NY) using a programmable micropipette puller (Sutter Instrument P-97, Novato, CA). The glass capillaries were loaded into the puller, where the central portion was heated by a platinum filament, softening the glass and allowing it to be pulled under tension to form a fine, tapered tip.

The specific parameters for pulling were optimized to achieve a visibly consistent tip diameter suitable for microinjection into zebrafish embryos. The needles were then loaded with filtered Rhodamine B solution at a concentration of 0.5 mg/mL, and the tip of the microcapillary needle was carefully broken with forceps to create a small, fine tip, calibrated to deliver ~1 nL per pedal press at a pressure of 5 psi.

Optical characterizations

SEM micrographs of the microneedles were captured using a TM4000 Tabletop SEM (Hitachi, Tokyo, Japan) and microneedle ODs were measured from the images using the TM4000 software (Hitachi). Brightfield micrographs were captured using a Zeiss Axio Observer Z1 optical microscope (Carl Zeiss Microscopy, LLC, White Plains, NY) and microneedle IDs were measured from the images using the ZEN software (Carl Zeiss Microscopy, LLC). All measurements were performed using $n = 10$ distinct microneedles corresponding to each needle type (i.e., $N = 30$ distinct microneedles in total).

Microfluidic burst-pressure experimentation

Microfluidic burst-pressure testing was performed using a Fluigent Microfluidic Control System (MFCS) and flow-rate platform coupled with OxyGEN software (Fluigent, France). DI water was inputted via fluorinated ethylene propylene tubing (Cole-Parmer, Vernon Hills, IL) and stainless-steel catheter couplers (20 ga., Instech, Plymouth Meeting, PA) connected to the opposing end of the capillary (i.e., without the printed microneedle) coupled to an inner-lok GC union tube adapter (Molex). Both input fluidic pressure and flow-rate data were collected using the OxyGEN software (Fluigent). The linear and cyclic microfluidic burst-pressure experiments were performed sequentially using $n = 10$ distinct microneedles corresponding to each printed needle type (i.e., $N = 20$ distinct microneedles in total). For linear burst-pressure testing, the input pressure was increased from 0 kPa to 200 kPa by 0.2 kPa increments every 0.2 s while monitoring the microneedle-capillary interface for indications of leakage or burst events under brightfield microscopy using an inverted microscope (AE31E, Motic) connected to a CCD Camera (Moticam Pro 285B, Motic). Thereafter, cyclic burst-pressure tests were performed by setting the input pressure at 110 kPa (to ensure an actual input pressure ≥100 kPa) for 2.5 s and then at 0 kPa for 2.5 s repeatedly for $n = 100$ cycles while continuing to monitor the microneedle-capillary interface for indications of leakage or burst events under brightfield microscopy using the Motic inverted microscope. All experiments were conducted under room temperature environment (~20–25° C).

Microinjection experiments with live zebrafish embryos

Wild type zebrafish (Danio rerio) of the AB strain were reared and maintained according to protocols approved by the Institutional Animal Care and Use Committee (IACUC) at the University of Maryland, Baltimore County. The zebrafish were kept in UV-irradiated, filtered water and exposed to a 12:12 light/dark cycle. Male and female fish were separated by a partition, which was removed following the first light to initiate spawning. Embryos were collected using a strainer, rinsed with system water, and then transferred to a Petri dish containing egg water (E3) media. The embryos were incubated in a 28 °C incubator for 24 h. The following morning, embryos were cleaned and staged according to the methods described by Kimmel et al.[104] The 20–24 h post-fertilization embryos were manually dechorionated using fine forceps under a stereomicroscope (Stemi 2000, Zeiss) equipped with a transmitted light base. Dechorionated embryos were then separated into individual Petri dishes—each containing 5 mL of system water—with 10 embryos per dish. Directly preceding injection, 50 µL of Tricaine (0.1 g/mL) was added to each dish to anesthetize the embryos.

Prior to microinjecting the zebrafish embryos, each microneedle was interfaced with a pipette holder (PLI-PH1, Harvard Apparatus, Holliston, MA) of the PLI-100 Medical System Pico-Injector (Harvard Apparatus). To interface the printed microneedles to the pipette holder, the open end of the capillaries (i.e., without a printed microneedle tip) was inserted into a thermoplastic micropipette (5-000-2005 Wiretrol II, Drummond Scientific Company, Broomall, PA) with a 0.49 mm ID and 1 mm OD, and then fixed with epoxy (Loctite HY4090, Henkel Corporation, Rocky Hill, CT). All injections were performed using an aqueous solution of rhodamine B (0.5 g/ml, Sigma-Aldrich, St. Louis, MO) in DI water with an input pressure of ~35 kPa applied using the PLI-100 Medical System Pico-Injector (Harvard Apparatus). For each trial, prior to the first microinjection, the corresponding microneedle was used to perform five pseudo-injections of aliquots atop a droplet of mineral oil (330779, Sigma-Aldrich, St. Louis, MO) on a microscope calibration slide, which were captured using a Monocular Max 300× microscope objective and a 41MP USB C-Mount Industry Microscope Camera Set (Hayear Electronics Co. Ltd., Shenzhen, China). ImageJ (NIH, Bethesda, MD) was used to measure the diameter of each droplet. Each microneedle was then used to perform 20 serial microinjections with the zebrafish embryos, with two injections performed on each embryo. Thereafter, a single pseudo-injection of an aliquot atop a droplet of mineral oil on a microscope calibration slide was performed and measured. These steps for the zebrafish embryo microinjections and pseudo-injection delivery volume measurements were repeated for a total of

100 serial microinjections and 10 delivery volume measurements (i.e., 5 measurements before microinjection, 1 measurement after each series of 20 zebrafish embryo microinjections) per trial. Each trial involved a distinct microneedle, with $n = 10$ trials per microneedle type and $N = 30$ trials in total.

Following each set of 20 serial microinjections of rhodamine B-labeled DI water into the zebrafish embryos, the corresponding embryos were collected ($n = 5$ groups per 100 serial microinjections) and lysed for fluorescence quantification. Specifically, after each set of 10 embryos was injected, they were immediately transferred to labeled Eppendorf tubes with 200 µL of fresh system water. Embryos were lysed using a Pestle Motor Mixer (Cole-Parmer), with the pestle being cleaned between each tube to prevent cross-contamination. Following lysis, 100 µL of the embryo lysate from each sample was transferred into a 96-well clear polystyrene, flat-bottom microplate. Non-injected embryos ($n = 5$ groups per 50 embryos) were also lysed and added to the 96-well plate for comparison. Rhodamine B fluorescence was measured using a SpectraMax M5 Microplate Reader (Molecular Devices) equipped with SoftMax Pro software. The settings for the measurement were as follows: Endpoint mode, fluorescence reading with excitation at 556 nm, and emission at 580 nm. The fluorescence intensity of each injected embryo group was quantified as the relative difference in intensity compared to that of the non-injected embryo groups. No outliers were removed from the data presented herein, and all microinjection trials were conducted under strictly controlled and standardized protocols—e.g., with regard to materials, embryo batches, number of embryos per trial, and applied injection pressures—to ensure experimental consistency.

Statistical analysis

Experimental results are presented in the text as mean ± S.D. The p values corresponding to differences in three or more samples were used to test any mean difference from the minimum mean via two independent samples Student's t tests. Differences with p values less than or equal to 0.05 were considered statistically significant.

Acknowledgments

We greatly appreciate the contributions of Rachel Brewster, Ian B. Rosenthal, Emmett Z. Freeman, Noemi Gonzalez, Michael Restaino, Matthew Kim, Sarah Young, Ladeja Robinson, Chloe Keller, Kay Htut, Allison Orlosky as well as members of the Bioinspired Advanced Manufacturing (BAM) Laboratory and Terrapin Works at the University of Maryland, College Park and the Micro/Nanofabrication Center at the Princeton Institute of Materials. This work was supported in part by U.S. National Institutes of Health (NIH) Award Numbers 1R41GM153053 and 1R41MH135827, U.S. National Science Foundation (NSF) Award Numbers 1943356 and 1938527, and Maryland Industrial Partnerships (MIPS) Award Numbers 6523 and 7422.

Author details

[1]Department of Mechanical Engineering, University of Maryland, College Park, MD 20742, USA. [2]Maryland Robotics Center, University of Maryland, College Park, MD 20742, USA. [3]Institute for Systems Research, University of Maryland, College Park, MD 20742, USA. [4]Department of Mechanical Engineering, University of Massachusetts, Amherst, MA 01003, USA. [5]Fischell Department of Bioengineering, University of Maryland, College Park, MD 20742, USA. [6]Department of Mathematics and Statistics, University of Maryland, Baltimore, MD 21250, USA. [7]Robert E. Fischell Institute for Biomedical Devices, University of Maryland, College Park, MD 20742, USA. [8]SeeTrue Technology, LLC., Rockville, MD 20852, USA

Conflict of interest

K. Rand-Yadin is Founding Director of SeeTrue Technology, LLC., which has a potential interest in commercializing the presented 3D microinjection needles.

Supplementary information The online version contains supplementary material available at https://doi.org/10.1038/s41378-025-01005-2.

Received: 13 January 2025 Revised: 24 April 2025 Accepted: 24 May 2025
Published online: 11 September 2025

References

1. Hamamoto, K., Umemura, Y., Makino, S. & Fukaya, T. Dynamic interplay between non-coding enhancer transcription and gene activity in development. *Nat. Commun.* **14**, 826 (2023).
2. Chen, B. et al. Maternal inheritance of glucose intolerance via oocyte TET3 insufficiency. *Nature* **605**, 761–766 (2022).
3. Tarazi, S. et al. Post-gastrulation synthetic embryos generated ex utero from mouse naive ESCs. *Cell* **185**, 3290–3306.e25 (2022).
4. Tokuoka, M., Maeda, K., Kobayashi, K., Mochizuki, A. & Satou, Y. The gene regulatory system for specifying germ layers in early embryos of the simple chordate. *Sci. Adv.* **7**, eabf8210 (2021).
5. Hanafy, A. S. et al. Subcellular analysis of blood-brain barrier function by micro-impalement of vessels in acute brain slices. *Nat. Commun.* **14**, 481 (2023).
6. Baptista, D. et al. Polymer film-based microwell array platform for long-term culture and research of human bronchial organoids. *Mater. Today Bio* **19**, 100603 (2023).
7. Zheng, Y. J., Dilbeck, M. D., Economides, J. R. & Horton, J. C. Permanent transduction of retinal ganglion cells by rAAV2-retro. *Exp. Eye Res.* **240**, 109793 (2024).
8. Tazin, N. et al. Transgenic expression in zebrafish embryos with an intact chorion by electroporation and microinjection. *Biotechnol. Rep.* **40**, e00814 (2023).
9. Lockery, S. R., Pop, S. & Jussila, B. Microinjection in C. elegans by direct penetration of elastomeric membranes. *Biomicrofluidics* **17**, 014103 (2023).
10. Holler, C., Taylor, R. W., Schambony, A., Möckl, L. & Sandoghdar, V. A paintbrush for delivery of nanoparticles and molecules to live cells with precise spatiotemporal control. *Nat. Methods* **21**, 512–520 (2024).
11. Saifullah, K. M. & Faraji Rad, Z. Sampling dermal interstitial fluid using microneedles: a review of recent developments in sampling methods and microneedle-based biosensors. *Adv. Mater. Interfaces* **10**, 2201763 (2023).
12. Li, M. et al. Methods for the generation of heritable germline mutations in the disease vector Culex quinquefasciatus using clustered regularly interspaced short palindrome repeats-associated protein 9. *Insect Mol. Biol.* **29**, 214–220 (2020).
13. Sahmi-Bounsiar, D. et al. Generation of infectious mimivirus virions through inoculation of viral DNA within *Acanthamoeba castellanii* shows involvement of five proteins, essentially uncharacterized. *Front. Microbiol.* **12**, 677847 (2021).
14. Chen, S. et al. Knock-In of a large reporter gene via the high-throughput microinjection of the CRISPR/Cas9 system. *IEEE Trans. Biomed. Eng.* **69**, 2524–2532 (2022).

15. Miyawaki, F. & Hasegawa, J. Development of vibratory microinjection system for instantaneous cell membrane piercing in cytoplasmic microinjection into fertilized eggs. *Actuators* **12**, 448 (2023).
16. Grüttner, J. et al. Trophozoite fitness dictates the intestinal epithelial cell response to Giardia intestinalis infection. *PLoS Pathog.* **19**, e1011372 (2023).
17. Shakoor, A. et al. Quality and quantity control of mitochondria injection into single cells with robot-aided micro-manipulation system. *IEEE Trans. Autom. Sci. Eng.* **21**, 1–12 (2023).
18. Wu, T.-H. et al. Mitochondrial transfer by photothermal nanoblade restores metabolite profile in mammalian cells. *Cell Metab.* **23**, 921–929 (2016).
19. Xu, C., Peng, B. & Liu, S. Using intra-brain drug infusion to investigate neural mechanisms underlying reward-seeking behavior in mice. *STAR Protoc.* **3**, 101221 (2022).
20. Griffin, W. C., Lopez, M. F., Woodward, J. J. & Becker, H. C. Alcohol dependence and the ventral hippocampal influence on alcohol drinking in male mice. *Alcohol* **106**, 44–54 (2023).
21. Hajduk, J., Szajna, K., Lisowski, B. & Rajfur, Z. The influence of microinjection parameters on cell survival and procedure efficiency. *Methods X* **10**, 102107 (2023).
22. Le, Q. A. et al. Comparison of the effects of introducing the CRISPR/Cas9 system by microinjection and electroporation into porcine embryos at different stages. *BMC Res. Notes* **14**, 7 (2021).
23. Maia, R., Carvalho, V., Lima, R., Minas, G. & Rodrigues, R. O. Microneedles in advanced microfluidic systems: a systematic review throughout lab and organ-on-a-chip applications. *Pharmaceutics* **15**, 792 (2023).
24. Pan, F. et al. Automated high-productivity microinjection system for adherent cells. *IEEE Robot. Autom. Lett.* **5**, 1167–1174 (2020).
25. Chen, L.-N. et al. High-survival rate after microinjection of mouse oocytes and early embryos with mRNA by combining a tip pipette and piezoelectric-assisted micromanipulator. *Front. Cell Dev. Biol.* **9**, 735971 (2021).
26. Esteves, S. C. & Varghese, A. C. Laboratory handling of epididymal and testicular spermatozoa: what can be done to improve sperm injections outcome. *J. Hum. Reprod. Sci.* **5**, 233–243 (2012).
27. Venken, K. J. T., Matinyan, N., Gonzalez, Y. & Dierick, H. A. Multiplexed transgenic selection and counterselection strategies to expedite genetic manipulation workflows using Drosophila melanogaster. *Curr. Protoc.* **3**, e652 (2023).
28. Parent, S. E., Luu, O., Bruce, A. E. E. & Winklbauer, R. Two-phase kinetics and cell cortex elastic behavior in Xenopus gastrula cell-cell adhesion. *Dev. Cell* **59**, 141–155.e6 (2024).
29. Rossi, F. & Gonzalez, C. Studying tumor growth in Drosophila using the tissue allograft method. *Nat. Protoc.* **10**, 1525–1534 (2015).
30. Giandomenico, S. L., Sutcliffe, M. & Lancaster, M. A. Generation and long-term culture of advanced cerebral organoids for studying later stages of neural development. *Nat. Protoc.* **16**, 579–602 (2021).
31. Zhou, Y., Sun, L., Watanabe, S. & Ando, T. Recent advances in the glass pipet: from fundament to applications. *Anal. Chem.* **94**, 324–335 (2022).
32. Miller, D. F. B., Holtzman, S. L. & Kaufman, T. C. Customized microinjection glass capillary needles for P-element transformations in Drosophila melanogaster. *Biotechniques* **33**, 366–375 (2002).
33. Qiao, G. et al. 3D printing-based frugal manufacturing of glass pipettes for minimally invasive delivery of therapeutics to the brain. *Neuroprotection* **1**, 35–42 (2023).
34. Gultom, V. D. N. Past, present and future prospect on microinjection gene transfer in aquaculture. *IOP Conf. Ser.* **1137**, 012040 (2023).
35. Xin, Y. & Duan, C. Microinjection of antisense morpholinos, CRISPR/Cas9 RNP, and RNA/DNA into zebrafish embryos. in *Hypoxia: Methods and Protocols*, (ed Huang, L. E.) 205–211. (Springer, 2018).
36. Castelletto M. L., Hallem E. A. Generating transgenics and knockouts in strongyloides species by microinjection. *J. Vis. Exp.* **176**, 63023 (2021).
37. Ordas, A. et al. Testing tuberculosis drug efficacy in a zebrafish high-throughput translational medicine screen. *Antimicrob. Agents Chemother.* **59**, 753–762 (2015).
38. Yang, L., Rojas, A. M. & Shiau, C. E. Liposomal clodronate-mediated macrophage depletion in the zebrafish model. *Bio-Protoc.* **11**, e3951 (2021).
39. Yang, L. et al. Drainage of inflammatory macromolecules from the brain to periphery targets the liver for macrophage infiltration. *eLife* **9**, e58191 (2020).
40. Ohde, T., Minemura, T., Hirose, E. & Daimon, T. Egg microinjection and efficient mating for genome editing in the firebrat Thermobia domestic. *J. Vis. Exp.* **164**, 61885 (2020).
41. Liwei, L. & Pisano, A. P. Silicon-processed microneedles. *J. Microelectromechanical Syst.* **8**, 78–84 (1999).
42. Ogai, N. et al. Enhanced immunity in intradermal vaccination by novel hollow microneedles. *Ski. Res. Technol.* **24**, 630–635 (2018).
43. Griss, P. & Stemme, G. Side-opened out-of-plane microneedles for microfluidic transdermal liquid transfer. *J. Microelectromechanical Syst.* **12**, 296–301 (2003).
44. Zhang, P. & Jullien, G. A. Microneedle arrays for drug delivery and fluid extraction. In *Proc. 2005 International Conference on MEMS, NANO and Smart Systems* 392–395 (IEEE, 2005).
45. Zhang, P., Dalton, C. & Jullien, G. A. Design and fabrication of MEMS-based microneedle arrays for medical applications. *Microsyst. Technol.* **15**, 1073–1082 (2009).
46. Li, Y. et al. Fabrication of sharp silicon hollow microneedles by deep-reactive ion etching towards minimally invasive diagnostics. *Microsyst. Nanoeng.* **5**, 41 (2019).
47. Karumuri, S. R. et al. Design, simulation and analysis of micro electromechanical system microneedle for micropump in drug delivery systems. *IET Nanobiotechnol.* **15**, 484–491 (2021).
48. Bodhale, D. W., Nisar, A. & Afzulpurkar, N. Structural and microfluidic analysis of hollow side-open polymeric microneedles for transdermal drug delivery applications. *Microfluid. Nanofluidics* **8**, 373–392 (2010).
49. Cárcamo-Martínez, Á. et al. Hollow microneedles: a perspective in biomedical applications. *Int. J. Pharm.* **599**, 120455 (2021).
50. Aldawood, F. K., Andar, A. & Desai, S. A comprehensive review of microneedles: types, materials, processes, characterizations and applications. *Polymers* **13**, 2815 (2021).
51. Gowthami, A., Sreeja, B. S. & Radha, S. Transdermal injection with microneedle devices in healthcare sector: materials, challenging fabrication methodologies, and its limitations. in *MEMS and Microfluidics in Healthcare: devices and Applications Perspectives* (eds Guha, K., Dutta, G., Biswas, A., & Srinivasa Rao K.) 183–201 (Springer Nature, 2023).
52. Larson, N. M. et al. Rotational multimaterial printing of filaments with sub-voxel control. *Nature* **613**, 682–688 (2023).
53. Orth, A. et al. Deconvolution volumetric additive manufacturing. *Nat. Commun.* **14**, 4412 (2023).
54. Sochol, R. D. et al. 3D printed microfluidic circuitry via multijet-based additive manufacturing. *Lab Chip* **16**, 668–678 (2016).
55. Somers, P. et al. The physics of 3D printing with light. *Nat. Rev. Phys.* **6**, 99–113 (2024).
56. Guo, Z., Ai, N., Ge, W. & Xu, Q. Design of an automated robotic microinjection system for batch injection of zebrafish embryos and larvae. *Microsyst. Nanoeng.* **10**, 20 (2024).
57. Guo, X. et al. Mechanical force characterization of living cells based on needle deformation. *Adv. Mater. Interfaces* **10**, 2300293 (2023).
58. Zhang, Y. et al. Genetic reporter for live tracing fluid flow forces during cell fate segregation in mouse blastocyst development. *Cell Stem Cell* **30**, 1110–1123.e9 (2023).
59. Loterie, D., Delrot, P. & Moser, C. High-resolution tomographic volumetric additive manufacturing. *Nat. Commun.* **11**, 852 (2020).
60. Hubbard, J. D. et al. Fully 3D-printed soft robots with integrated fluidic circuitry. *Sci. Adv.* **7**, eabe5257 (2021).
61. Sanchez Noriega, J. L. et al. Spatially and optically tailored 3D printing for highly miniaturized and integrated microfluidics. *Nat. Commun.* **12**, 5509 (2021).
62. Detamornrat, U., McAlister, E., Hutton, A. R. J., Larrañeta, E. & Donnelly, R. F. The role of 3D printing technology in microengineering of microneedles,. *Small* **18**, 2106392 (2022).
63. Román-Manso, B., Weeks, R. D., Truby, R. L. & Lewis, J. A. Embedded 3D printing of architected ceramics via microwave-activated polymerization. *Adv. Mater.* **35**, 2209270 (2023).
64. Gauci, S. C. et al. Photochemically activated 3D printing inks: current status, challenges, and opportunities. *Adv. Mater.* **36**, 2306468 (2024).
65. Lamont, A. C., Alsharhan, A. T. & Sochol, R. D. Geometric determinants of in-situ direct laser writing. *Sci. Rep.* **9**, 394 (2019).
66. Weidinger, B. et al. 3D printing hierarchically nano-ordered structures. *Adv. Sci.* **10**, 2302756 (2023).
67. Lölsberg, J. et al. 3D nanofabrication inside rapid prototyped microfluidic channels showcased by wet-spinning of single micrometre fibres. *Lab Chip* **18**, 1341–1348 (2018).

68. Alsharhan, A. T., Acevedo, R., Warren, R. & Sochol, R. D. 3D microfluidics via cyclic olefin polymer-based in-situ direct laser writing,. *Lab Chip* **19**, 2799–2810 (2019).
69. Smith, G. L. et al. Spider-inspired, fully 3D-printed micro-hydraulics for tiny, soft robotics. *Adv. Funct. Mater.* **33**, 2207435 (2023).
70. Szeto, B. et al. Novel 3D-printed hollow microneedles facilitate safe, reliable, and informative sampling of perilymph from guinea pigs. *Hear. Res.* **400**, 108141 (2021).
71. Dewandre, A., Rivero-Rodriguez, J., Vitry, Y., Sobac, B. & Scheid, B. Microfluidic droplet generation based on non-embedded co-flow-focusing using 3D printed nozzle. *Sci. Rep.* **10**, 21616 (2020).
72. Barbot, A., Wales, D., Yeatman, E. & Yang, G.-Z. Microfluidics at fiber tip for nanoliter delivery and sampling. *Adv. Sci.* **8**, 2004643 (2021).
73. Knoška, J. et al. Ultracompact 3D microfluidics for time-resolved structural biology. *Nat. Commun.* **11**, 657 (2020).
74. Trautmann, A., Roth, G.-L., Nujiqi, B., Walther, T. & Hellmann, R. Towards a versatile point-of-care system combining femtosecond laser generated microfluidic channels and direct laser written microneedle arrays. *Microsyst. Nanoeng.* **5**, 6 (2019).
75. Barbot, A., Power, M., Seichepine, F. & Yang, G.-Z. Liquid seal for compact micropiston actuation at the capillary tip. *Sci. Adv.* **6**, eaba5660 (2020).
76. Acevedo R. et al. 3D nanoprinted external microfluidic structures via ex situ direct laser writing, In *Proc. 2021 IEEE 34th International Conference on Micro Electro Mechanical Systems (MEMS)*, 10–13 (IEEE, 2021).
77. Sarker, S. et al. 3D-printed microinjection needle arrays via a hybrid DLP-direct laser writing strategy. *Adv. Mater. Technol.* **8**, 2201641 (2023).
78. Power, M., Barbot, A., Seichepine, F. & Yang, G.-Z. Bistable, pneumatically actuated microgripper fabricated using two-photon polymerization and oxygen plasma etching. *Adv. Intell. Syst.* **5**, 2200121 (2023).
79. Oka, A. et al. Alopecia areata susceptibility variant in MHC region impacts expressions of genes contributing to hair keratinization and is involved in hair loss. *eBioMedicine* **57**, 102810 (2020).
80. Than, A., Zan, P. & Chen, P. Transdermal theranostics. *VIEW* **1**, e21 (2020).
81. Peglion, F., Coumailleau, F. & Etienne-Manneville, S. Live imaging of microtubule dynamics in glioblastoma cells invading the zebrafish brain. *J. Vis. Exp.* **185**, e64093 (2022).
82. Campo, E. M. et al. Focus ion beam micromachined glass pipettes for cell microinjection. *Biomed. Microdevices* **12**, 311–316 (2010).
83. Muñoz-Sánchez, B. N., Gañán-Calvo, A. M. & Cabezas, M. G. A new fire shaping approach to produce highly axisymmetric and reproducible nozzles. *J. Mater. Process. Technol.* **270**, 241–253 (2019).
84. Yaul, M., Bhatti, R. & Lawrence, S. Evaluating the process of polishing borosilicate glass capillaries used for fabrication of in-vitro fertilization (iVF) micropipettes. *Biomed. Microdevices* **10**, 123–128 (2008).
85. Elias Abi-Ramia Silva, T., Kohler, S., Bartzsch, N., Beuschlein, F. & Güntner, A. T. 3D-printed polymer hollow microneedles on microfluidic platforms for minimally invasive interstitial fluid extraction. *Cell Biomater.* **1**, 100008 (2025).
86. Calikoglu, A., Lux, F., Taege, Y., Zappe, H. & Ataman, Ç. 3D nano-printed bistable microlens actuator for reconfigurable micro-optical systems. *Adv. Funct. Mater.* **34**, 2408867 (2024).
87. Xu, X. et al. 3D-microprinted PDMS-based microfluidic vessels for organ-on-a-chip applications. In *Proc. 2024 IEEE 37th International Conference on Micro Electro Mechanical Systems (MEMS)* 221–224 (IEEE, 2024).
88. Xu, X. et al. 3D nanoprinting of PDMS microvessels with tailored tortuosity and microporosity via direct laser writing, *Lab Chip* https://doi.org/10.1039/D4LC01051E (2025).
89. Gissibl, T., Thiele, S., Herkommer, A. & Giessen, H. Two-photon direct laser writing of ultracompact multi-lens objectives. *Nat. Photonics* **10**, 554 (2016).
90. Dietrich, P. I. et al. In situ 3D nanoprinting of free-form coupling elements for hybrid photonic integration. *Nat. Photonics* **12**, 241–247 (2018).
91. Power, M., Thompson, A. J., Anastasova, S. & Yang, G.-Z. A monolithic force-sensitive 3d microgripper fabricated on the tip of an optical fiber using 2-photon polymerization. *Small* **14**, 1703964 (2018).
92. Gade, S. et al. Hollow microneedles for ocular drug delivery. *J. Control. Release* **371**, 43–66 (2024).
93. Zhu, H. et al. 3D printing of drug delivery systems enhanced with micro/nano-technology. *Adv. Drug Deliv. Rev.* **216**, 115479 (2025).
94. Levy, J. A., Straker, M. A., Colton, A., Sochol, R. D. & Ghodssi, R. Anchoring injector for prolonged dosing of drugs in the gastrointestinal tract, In *Proc. 2024 IEEE 37th International Conference on Micro Electro Mechanical Systems (MEMS)* 417–420 (IEEE, 2024).
95. Kim, J., Jeong, J., Jo, J. K. & So, H. Hollow microneedles as a flexible dosing control solution for transdermal drug delivery. *Mater. Today Bio* **32**, 101754 (2025).
96. Sagot, M. et al. Functionality integration in stereolithography 3D printed microfluidics using a "print-pause-print" strategy. *Lab Chip* **24**, 3508–3520 (2024).
97. Dinh, M. T. P. et al. Separation of platelets by size in a microfluidic device based on controlled incremental filtration. *Lab Chip* **24**, 913–923 (2024).
98. Zhang, J. et al. Advancements in microfluidic technology for rapid bacterial detection and inflammation-driven diseases, *Lab Chip* https://doi.org/10.1039/D4LC00795F (2025).
99. Felix, B. M. et al. An approach for 3D microprinting soft robotic surgical tools at 1.5 french length scales for endovascular interventions. In *Proc. 2024 IEEE 7th International Conference on Soft Robotics (RoboSoft)* 386–391 (IEEE, 2024).
100. Colton, A. et al. Toward "S"-shaped 3D-printed soft robotic guidewires for pediatric patent ductus arteriosus endovascular interventions. In *Proc. 2024 IEEE 7th International Conference on Soft Robotics (RoboSoft)* 965–970 (IEEE, 2024).
101. Mainik, P., Spiegel, C. A. & Blasco, E. Recent advances in multi-photon 3D laser printing: active materials and applications. *Adv. Mater.* **36**, 2310100 (2024).
102. Young, O. M., Xu, X., Sarker, S. & Sochol, R. D. Direct laser writing-enabled 3D printing strategies for microfluidic applications. *Lab Chip* **24**, 2371–2396 (2024).
103. Liu, T. et al. Ultrahigh-printing-speed photoresists for additive manufacturing. *Nat. Nanotechnol.* **19**, 51–57 (2024).
104. Kimmel, C. B., Ballard, W. W., Kimmel, S. R., Ullmann, B. & Schilling, T. F. Stages of embryonic development of the zebrafish. *Dev. Dyn.* **203**, 253–310 (1995).